ACS NANO

www.acsnano.org

ARTICLE

Tunable Hybridized Morphologies Obtained through Flash Joule Heating of Carbon Nanotubes

Paul A. Advincula, Jacob L. Beckham, Chi Hun Choi, Weiyin Chen, Yimo Han, Dmitry V. Kosynkin, Alexander Lathem, Alvaro Mayoral, Miguel Jose Yacaman,* and James M. Tour*

Cite This: *ACS Nano* 2023, 17, 2506–2516

Read Online

ACCESS | Metrics & More | Article Recommendations | Supporting Information

ABSTRACT: **Hybrid carbon nanomaterials, such as those that incorporate carbon nanotubes into graphene sheets, have been found to display interesting mechanical and electrical properties because of their covalent bonding and $\pi-\pi$ stacking domains. However, synthesis of these hybrid materials is limited by the high energetic cost of techniques like chemical vapor deposition. Here, we demonstrate the solvent- and gas-free synthesis of a 2D carbon nanotube/graphene network through flash Joule heating of pristine carbon nanotubes. The relative proportion of each morphology in the hybrid material can be tuned by varying the pulse time, as confirmed by Raman spectroscopy and microscopy. Triboindentation of epoxy composites made with the hybrid material shows increases of 162% and 64% to the hardness and Young's modulus, respectively, compared with the neat epoxy. These results demonstrate that flash Joule heating can be used to inexpensively convert carbon nanotubes into a hybrid network of nanotubes and graphene for use as an effective reinforcing additive in epoxy composites.**

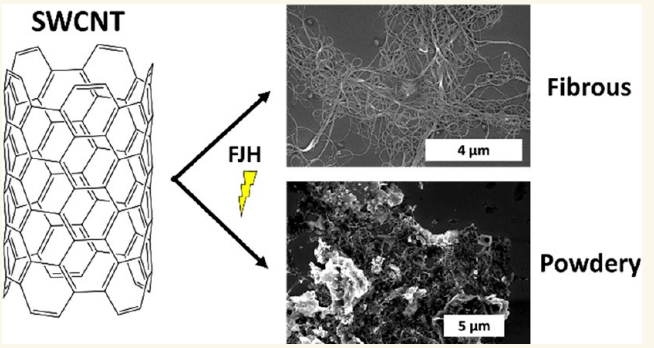

KEYWORDS: *carbon nanotubes, flash Joule heating, hybrid morphologies, flash graphene, composites, unzipping, cross-linking*

Carbon nanotubes (CNT) that are unzipped to graphene nanoribbons (GNR) have interesting mechanical and electrical properties, which makes them suitable for a variety of applications, especially as conductive fillers that allow for percolation at low loadings because of their high aspect ratios and conductivity.[1−4] Other applications include electrocatalysis,[5] batteries,[6,7] and nanoscale devices.[8,9] However, synthesis of these distinct morphologies relies on harsh oxidative[10] and reductive methods,[11] self-assembly,[12] and chemical vapor deposition,[13] which have limited their use on a larger scale. Other techniques use high-velocity impact to unzip CNT through mechanical collisions.[14]

Such unzipping mechanisms can be used to form hybrid materials consisting of CNT, GNR, and graphene in varying combinations. These materials combine the properties of each morphology into a single material. For example, conjoined CNT and GNR results in mechanical interlocking at the junction between the two morphologies, thereby improving the material's mechanical properties and its ability to dissipate energy.[15] Integrating CNT into graphene results in significant toughening of the graphene.[16] Hybrid materials incorporating various carbon morphologies have been demonstrated for use in composites,[17] energy storage,[18] and field-emission emitters.[19−21]

Flash Joule heating (FJH) has been shown to be a useful method for obtaining diverse morphologies of 2D materials, such as fluorinated nanodiamonds,[22] turbostratic boron nitride,[23] or flash graphene.[24−27] It has also been used to fuse together adjacent carbon nanofibers, thereby forming graphitic carbon bonds that lead to a 3D continuous carbon network.[28] Previous reports have shown that defect formations can be responsible for covalent bonding between nanotubes.[29] Here, FJH is used to convert single-walled CNT (SWCNT) rapidly and inexpensively into flash graphene (FG), cross-linked GNR, and hybrid materials that incorporate both

Received: October 11, 2022
Accepted: January 19, 2023
Published: January 24, 2023

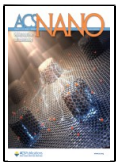

https://doi.org/10.1021/acsnano.2c10125
ACS Nano 2023, 17, 2506–2516

morphologies, as determined through Raman spectroscopy and electron microscopy. The efficacy of these nanomaterials as reinforcing additives is further demonstrated in epoxy composites. This technique could enable preparation of GNR/graphene covalent composite blends on a much larger scale than has previously been achieved, thereby allowing their use in a wider range of applications.

RESULTS/DISCUSSION

SWCNT are compressed between copper electrodes within a quartz tube, as shown in Figure 1a. The resistance of the SWCNT prior to compression in the FJH jig is 0.3−1.0 Ω, which enables sufficient Joule heating for the process. Resistance of the SWCNT sample can be modulated by changing the pressure exerted on the sample by the jig, thereby enabling a consistent resistance of 0.3 Ω prior to FJH for each batch. Current is passed through this feedstock during the FJH process, which converts the starting materials into two products that are separated using a #60 sieve. A variety of different morphologies are then visible, as seen in Figure 1b, which range between pristine SWCNT (200-50-f, 200-1000-f), cross-linked GNR (200-50-p, 200-1000-p), and FG morphologies (200-2000-p, 200-2000-f) (see Figure 1 caption for labeling description).

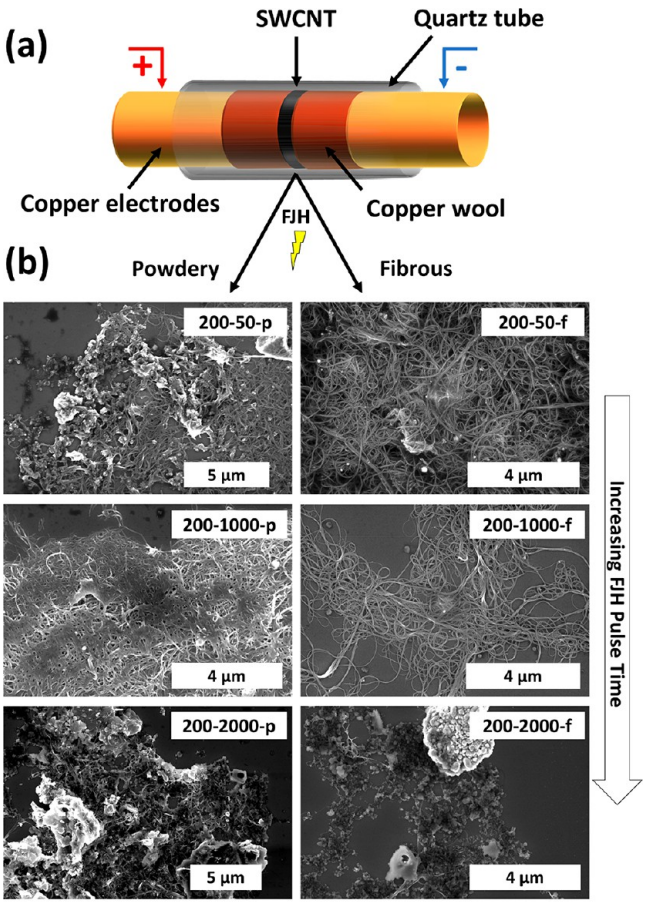

Figure 1. (a) Schematic of the FJH process. (b) Schematic illustration of the morphological change undergone by SWCNT with varying FJH pulse time. Samples are labeled using the "*X-Y-Z*" format, where *X* is the pulse voltage in V, *Y* is the pulse time in ms, and *Z* denotes whether the sample is powdery ("p") or fibrous ("f").

The FJH process affords control over a variety of parameters, such as the pulse time over which the voltage is applied. Allowing the pulse to continue over 1000 ms results in a high initial current of ∼700 A, followed by a much lower current for the remainder of the pulse (Figure 2a). Shortening the pulse to 100 or 50 ms, as shown in Figure 2b,c, respectively, arrests the progress of the FJH pulse without changing the peak current, thereby lowering the overall energy density of the pulse applied to the feedstock. Previous reports have shown that varying the pulse time can greatly alter the morphology of the resulting materials.[27,30]

During FJH of the SWCNT, the feedstock forms a variety of morphologies. Raman spectroscopy is a powerful technique for analysis of the different morphologies that are present. It can be used to analyze the formation of FG[31] and unzipped SWCNT.[5] There are three main peaks observed in these spectra: D (∼1350 cm^{-1}), G (∼1580 cm^{-1}), and 2D (∼2700 cm^{-1}). In typical Raman spectral profiles, the D band can be attributed to the presence of defects or graphene edges, where the intensity of the band is proportional to the concentration of these features. The G band arises in response to an in-plane phonon mode commonly observed in graphitic carbon. Finally, the 2D band appears from the overtone of the in-plane transverse optic branch. The I_D/I_G and I_{2D}/I_G ratios allow for assessment of the quality of the resulting material.

These results demonstrate that as pulse time increases, the I_D/I_G and I_{2D}/I_G ratios also increase, thereby indicating the presence of a greater proportion of FG and unzipped SWCNT than with pristine SWCNT (Figure 2d). A sample of pristine SWCNT has an average I_D/I_G and I_{2D}/I_G ratio of 0.035 and 0.089, respectively. After 50 ms of FJH, the I_D/I_G and I_{2D}/I_G ratios increase to 0.239 and 0.600, respectively. At 100 ms, the values of I_D/I_G and I_{2D}/I_G decrease and increase to 0.182 and 0.618, respectively. Finally, after 1000 ms, the I_D/I_G and I_{2D}/I_G ratios reach the values of 0.458 and 0.609, respectively. The large increase in I_{2D}/I_G and I_D/I_G ratios upon FJH of pristine SWCNT is indicative of a change in morphology from SWCNT to FG and GNR.

The percentage of spectra reminiscent of the spectral character of graphene was quantified as the "graphene yield" (see Methods). Prior to FJH, none of these spectra qualified as graphene. At 50 ms, 68% are counted as graphene. At 100 ms, 74% meet the criteria. Finally, at 1000 ms, 78% of the spectra qualify as graphene. Ergo, variation of the FJH pulse time allows for control over the degree of SWCNT conversion into graphene.

Figure S1 tracks the temperature of the FJH process as a function of time (see Methods). The crosshairs indicate how long the temperature was above 2500 K for each sample. During the 50 ms pulse, the temperature of the sample exceeded 2500 K for 31.6 ms (Figure S1a). With a pulse time of 75 ms, the temperature exceeded 2500 K for 41.2 ms (Figure S1b). Except for the 100 ms pulse, the amount of time that the sample exceeded 2500 K increased as the pulse time was increased. Setting the pulse time to 100, 1000, 1500, and 2000 ms caused the sample's temperature to exceed 2500 K for 32.2, 56.8, 111.3, and 155.0 ms, respectively (Figures S1c−f). These measurements (Figure S1) indicate that heating occurs over a longer period as pulse time increases, which likely facilitates the formation of FG, whereas the shorter pulses and

https://doi.org/10.1021/acsnano.2c10125
ACS Nano 2023, 17, 2506−2516

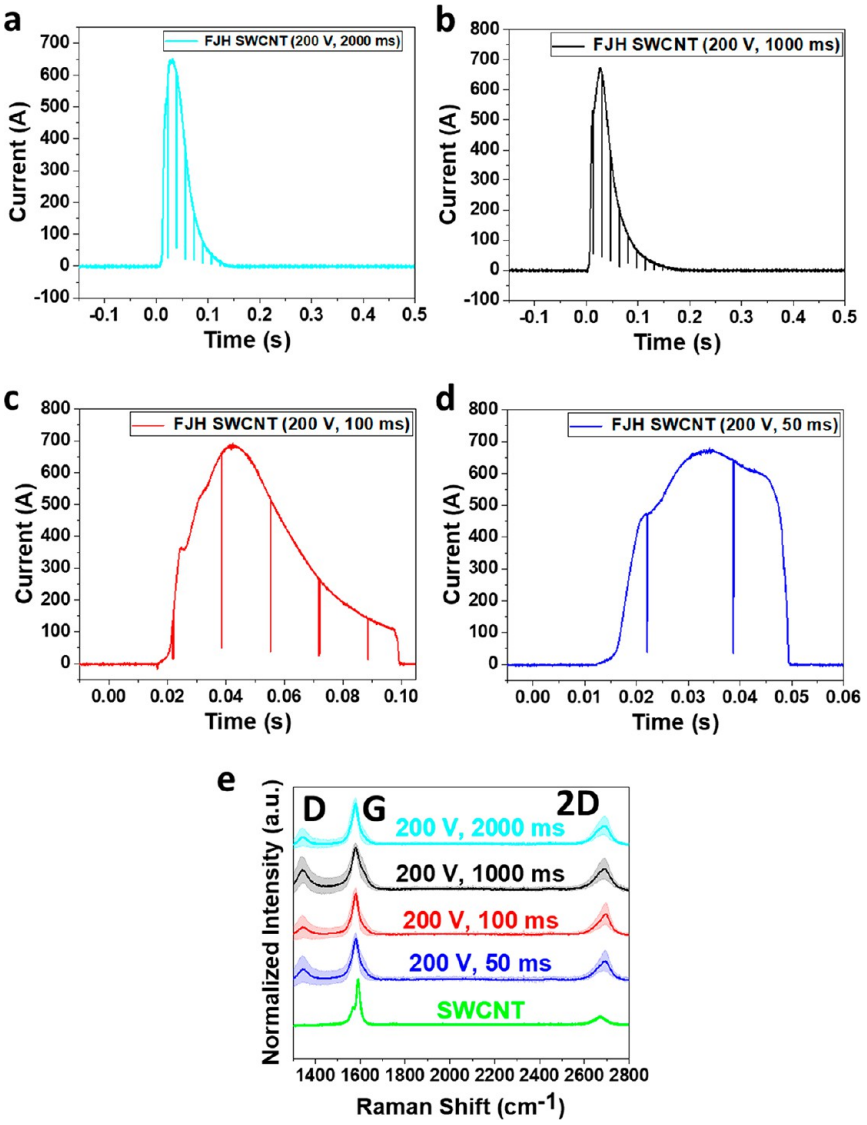

Figure 2. FJH parameters and Raman analyses of the products, prior to separation into fibrous and powdery portions. (a–d) Current as a function of time for FJH Meijo SWCNT with varying pulse times. Vertical lines are due to noise from the power supply to the Hall effect sensor used in current measurement, which occurs at 120 Hz. (e) Average Raman spectra of the resulting materials and pristine SWCNT. The shaded region depicts the standard deviation of the average spectra (N = 100). All spectra, except for "SWCNT," are FJH SWCNT listed with the pulse voltage and pulse time used during the FJH reaction.

heating times favor unzipping of SWCNT without coalescence into FG.

Previous reports show that peak temperature depends greatly on the peak current.[30] Given that the maximum current for the pulses are between 650 and 700 A, the maximum temperature achieved for each pulse is likely similar.

Upon FJH of the SWCNT, the sample comprises black powder, as well as stringy bundles of fibers, similar to the initial SWCNT feedstock. Average Raman spectra of the fibrous portion indicate that SWCNT are the dominant morphology in this portion of the sample, given the high frequency with which radial breathing modes (RBM) appear between 100 and 200 cm^{-1} (Figure S2a) and the presence of a shoulder on the 2D peak (Figure S2b). At higher pulse times, the increase in I_{2D}/I_G ratios indicates the presence of FG or GNR (Figure 3a and Figure S2e). Average Raman spectra of the powdery portion indicate that FG is the dominant morphology within this portion of the sample (Figure 3b). The low intensities of RBM (Figure S2c) and increased I_D/I_G ratios (Figure S2d) of the powdery portions also indicate that either FG or GNR is the dominant morphology in the powdery portion of the sample (Figure S2f). Measurement of the weight of each portion of the sample indicates that as the pulse time increases, the majority of the SWCNT are converted into FG (Figure 3c). At a pulse time of 25 ms, the sample does not undergo conversion, and all the material is considered fibrous, pristine SWCNT, as determined by Raman analysis. A pulse time of 50 ms is already sufficient to convert ~80% of the material into FG/GNR, with nearly 100% of the material being converted at a pulse time of 2000 ms.

As the pulse time increases, the I_{2D}/I_G ratio also increases, thereby indicating that the proportion of pristine SWCNT decreases, while the proportion of GNR/FG increases in both samples (Figure 3d). As the pulse time increases, the I_D/I_G ratios also increase, thereby indicating that the proportion of pristine SWCNT begins to decrease (Figure 3e).

https://doi.org/10.1021/acsnano.2c10125
ACS Nano 2023, 17, 2506–2516

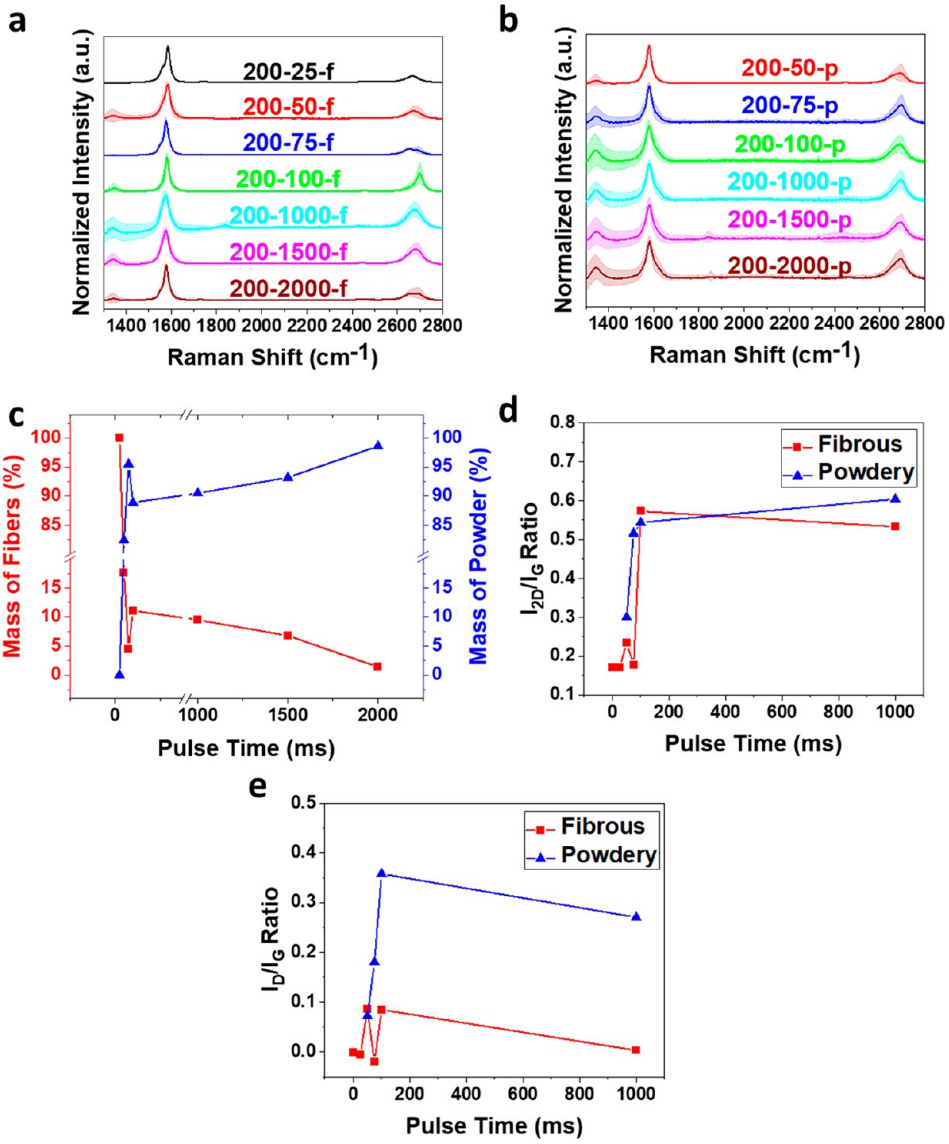

Figure 3. Average Raman spectra of the (a) fibrous and (b) powdery portions of FJH Meijo SWCNT because of varying pulse time. The shaded portion represents the standard deviation of $N = 100$ spectra. (c) Change in fibrous and powdery proportions as pulse time increases. Average (d) I_{2D}/I_G ratio and (e) I_D/I_G ratio as a function of varying pulse time.

The sample 200-1000-p is made of long structures that are clearly unzipped nanotubes as GNR (Figure 4a–c). These are especially visible in Figure 4d. In some regions, the graphene takes on a more ordered form (Figure 4e), whereas in others, graphene appears as strips with rotational disorder in a mosaic-type structure (Figure 4f). Compared with pristine Meijo SWCNT, the FJH materials have much rougher edges and display the formation of graphene films between bundles (Figure S3). These images demonstrate that varying degrees of graphene disorder are accessible within the same sample. During FJH, it is likely that C–C bonds within the nanotube are broken because of the high temperature of the process. These C atoms can then coalesce and cross-link with nearby SWCNT, similar to carbon welding from Joule heating.[28] Given enough time, these can rearrange into graphene to varying degrees, which results in a mix of SWCNT, unzipped SWCNT, and FG with covalent junctions. Longer times result in graphitization. Larger tube diameters will likely result in larger cross-linked areas and a greater degree of unzipping. Previous reports of CNT unzipping through oxidative and reductive splitting showed that CNT with smaller diameters were more difficult to fully unzip.[9]

HAADF-STEM images of the fibrous and powdery materials suggest the covalent connections forming the rebar structure of the CNT–graphene blend. Several junctions are visible between the filmlike graphene and the CNT in the powdery portion (Figure 5a,b), as well as in the fibrous portion (Figure 5c,d), albeit with much lower frequency. These images demonstrate that a hybrid material is formed with CNT unzipping and forming into GNR films to varying degrees. HRTEM images of the covalent junctions in the 200-100-f samples can be found in Figure S4.

SEM images show that as pulse time increases, the proportion of FG begins to increase (Figure 6a–f). The formation of cross-linked GNR networks is also apparent, especially in Figure 6d. At increased pulse times, larger sheet FG morphologies begin to appear and predominate. SEM images of 200-50-p shows that pristine SWCNT predominate,

https://doi.org/10.1021/acsnano.2c10125
ACS Nano 2023, 17, 2506–2516

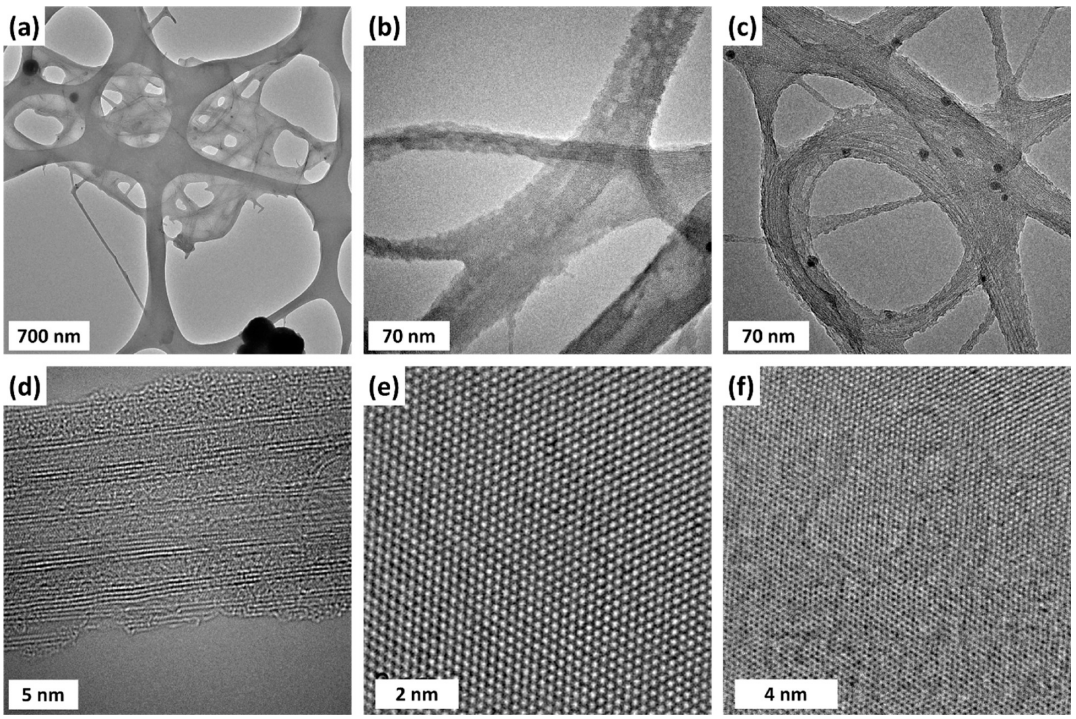

Figure 4. (a–d) TEM images of hybrid materials and aberration-corrected HRTEM images of (e) ordered and (f) rotationally disordered graphene areas of 200-1000-p.

but some cross-linking is apparent, along with FG flakes <50 nm in lateral diameter (Figure 6a). A few larger flakes up to 250 nm are visible, as well. At 75 ms, larger areas of cross-linking begin to appear, with flakes of FG incorporated into the structure (Figure 6b). After 100 ms, FG flakes with diameters of 5 to 10 μm are visible with pristine and cross-linked SWCNT (Figure 6c). A pulse of 1000 ms results in powdery material with high degrees of cross-linking, thereby resulting in a matted network of SWCNT (Figure 6d). Long pulse times of 1500 and 2000 ms display much larger flakes of 10 to 20 μm with matted networks of cross-linked SWCNT and smaller FG flakes (Figure 6e,f). Additional SEM images of the powdery portions can be found in Figure S5.

SEM images show that the fibrous material largely appears to be comprised of pristine SWCNT, with some GNR present (Figure 6g–l). At pulse times below 2000 ms, pristine bundles of SWCNT constitute most of the morphologies present. This trend persists until 2000 ms, at which point FG morphologies are the only ones visible. Additional SEM images of the fibrous portions can be found in Figure S6.

TEM images of the powdery portions indicate that GNR are present as the pulse time increases, along with the formation of FG morphologies (Figure 7a–f). At 50 ms, small flakes of FG are visible with bundles of SWCNT (Figure 7a). Junctions between the bundles of SWCNT can be seen at 75 ms (Figure 7b). Unzipping of SWCNT into GNR can also be observed after 100 ms (Figure 7c). Even greater degrees of unzipping are visible at 1000 and 1500 ms, especially at the junctions between the SWCNT bundles (Figure 7d,e). Finally, a film of FG with incorporated SWCNT can be seen at 2000 ms (Figure 7f). Additional TEM images of the powdery portions can be found in Figure S7.

TEM images of the fibrous portions show that pristine SWCNT predominate at lower pulse times (Figure 7g–j), while at higher pulse times of 1500 and 2000 ms, GNR and FG appear, as well (Figure 7k–l). Additional TEM images of the fibrous portions can be found in Figure S8.

Triboindentation of composites made with FJH SWCNT as reinforcing additives demonstrates that an addition of either the fibrous or powdery proportion enhances the mechanical properties of the material (Figure 8a). An addition of 1 wt % of the powdery portion results in 162% and 64% increases to the hardness and Young's modulus, respectively. An addition of 1 wt % of the fibrous portion results in 88% and 42% increases in the hardness and Young's modulus, respectively. Greater enhancement is observed when using the powdery portion. Since electron microscopy analyses indicate that both powdery and fibrous materials contain hybrid morphologies of graphene and SWCNT, we attribute the greater enhancement of mechanical properties using powdery material to the enhanced dispersibility of the powdery material, as determined by UV–vis spectroscopy (Figure S9).

An addition of CG and SWCNT also leads to increases in mechanical properties, albeit less than the FJH SWCNT materials (Figure 8b). A loading of 0.25 wt % SWCNT was used because of the difficulty of dispersing a higher wt % of the low-density SWCNT in the epoxy. An addition of SWCNT leads to increases of 133% and 24% in the hardness and Young's modulus, respectively. The greater enhancement of FJH SWCNT compared with pristine SWCNT can likely be attributed to the ease with which the FJH materials can be dispersed. Furthermore, covalent cross-linking of SWCNT likely locks the SWCNT from sliding. The use of 0.5 and 1 wt % CG in the epoxy results in the same increases of 101% and 27% to the hardness and Young's modulus, respectively.

CONCLUSIONS

SWCNT have been subjected to FJH under a variety of pulse times and separated into powdery and fibrous proportions with a #60 sieve. Raman and electron microscopy indicate that as

https://doi.org/10.1021/acsnano.2c10125
ACS Nano 2023, 17, 2506–2516

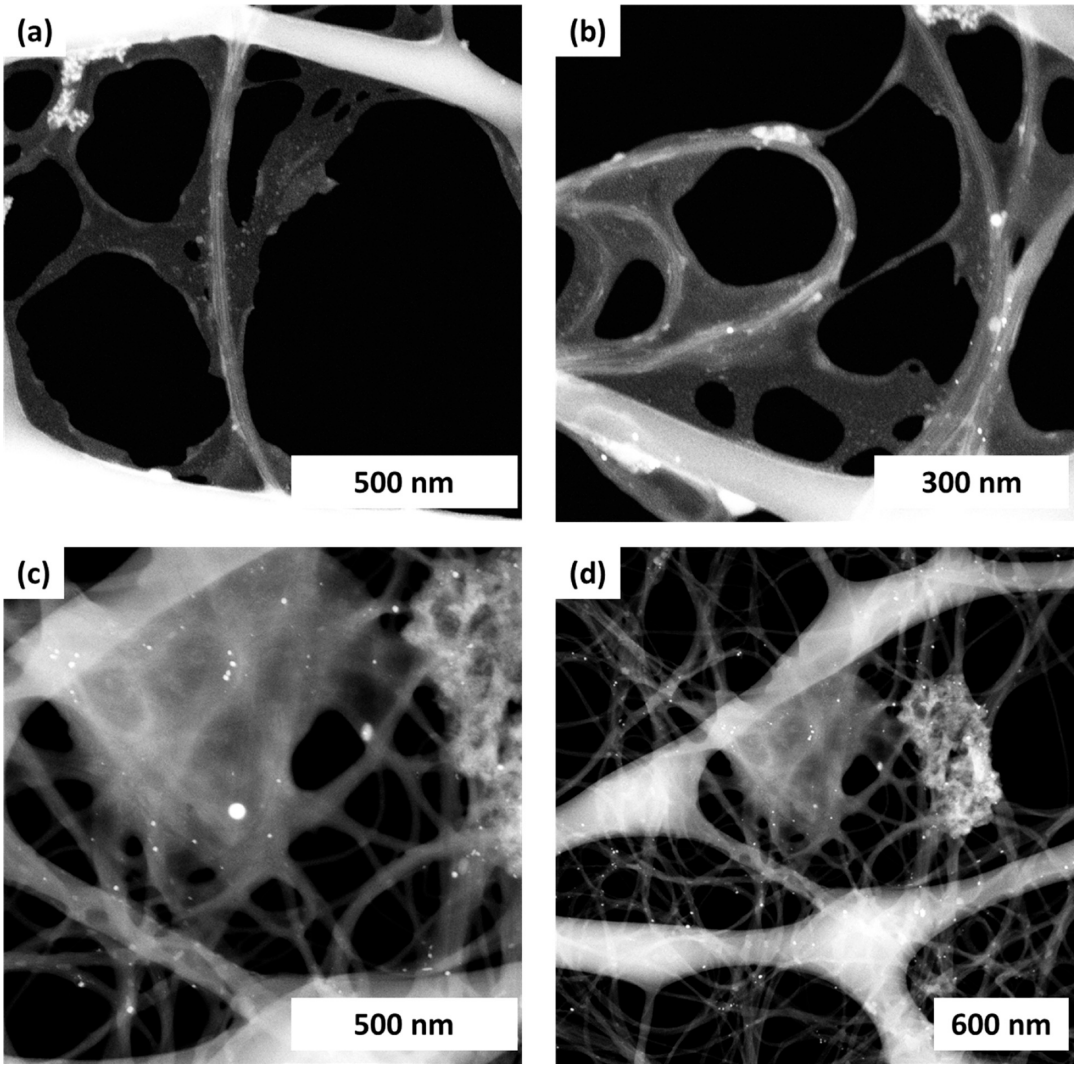

Figure 5. HAADF-STEM images of (a,b) 200-100-p and (c,d) 200-100-f.

pulse time increases, the ratio of powdery material to fibrous material begins to increase, which corresponds to a decrease in the number of pristine carbon nanotubes with an increase in GNR content. Additionally, the powdery portion displays FG morphologies, which becomes the dominant morphology at extended pulse times of 1000 to 2000 ms. In the fibrous portion, pristine SWCNT are the dominant morphology, along with a lower proportion of GNR. This technique offers tunable control over the different carbon morphologies in the sample by varying the pulse time. The different morphologies can then be separated using a sieve to yield a range of materials, including pristine SWCNT, unzipped SWCNT that are GNR, and FG. Finally, these materials can be used as a reinforcing additive to enhance the mechanical properties of epoxy composites. The Young's modulus and hardness can be increased by 64% and 162%, respectively, through an addition of 1% of the powdery materials. The Young's modulus and hardness can also be increased by 42% and 88%, respectively, by adding 1% of the fibrous material. These results demonstrate that flash Joule heating can inexpensively convert pristine CNT into a hybrid network of CNT/graphene that can effectively reinforce epoxy composites.

METHODS/EXPERIMENTAL

Materials. SWCNT (eDIPS, EC1.5) were purchased from Meijo and used as received. An epoxy resin, designated as DER 736 (Lot #: BCBM6627V), was obtained from Millipore-Sigma and used as received. 1,5-Diamino-2-methylpentane (Dytek A, Lot #: SHBG9920V) was obtained from Millipore-Sigma and used as received. Pluronic F-127 (Lot #: BCCF5250) was obtained from Millipore-Sigma and used as received. Commercial graphene (CG) was obtained from Tianyuan Empire Materials & Technology Limited and used as received.

Flash Joule Heating. The SWCNT were subjected to FJH using a pulse voltage of 200 V and varying pulse times between 25 and 2000 ms. In each FJH reaction was used 15 mg of SWCNT. The resulting FJH CNTs were separated using a #60 sieve. Materials smaller than this were designated as the powdery material, while materials larger than this size were designated as the fibrous material.

Raman Spectroscopy. Raman spectra were collected using a Renishaw inVia confocal Raman microscope with a 532 nm laser. A laser power of 5 mW was used with a 50× objective lens to scan the materials in the range of 1300−2800 cm^{-1}. Large-area Raman mappings were collected to assess the crystallinity and morphology of the FJH SWCNT. The spectra were then analyzed using a custom-written Python script using the RamPy package. The spectra were background-corrected, and a Savitsky−Golay filter was applied to smooth the spectra. The graphene yield and peak ratios were quantified, with spectra qualifying as graphene upon meeting three

https://doi.org/10.1021/acsnano.2c10125
ACS Nano 2023, 17, 2506−2516

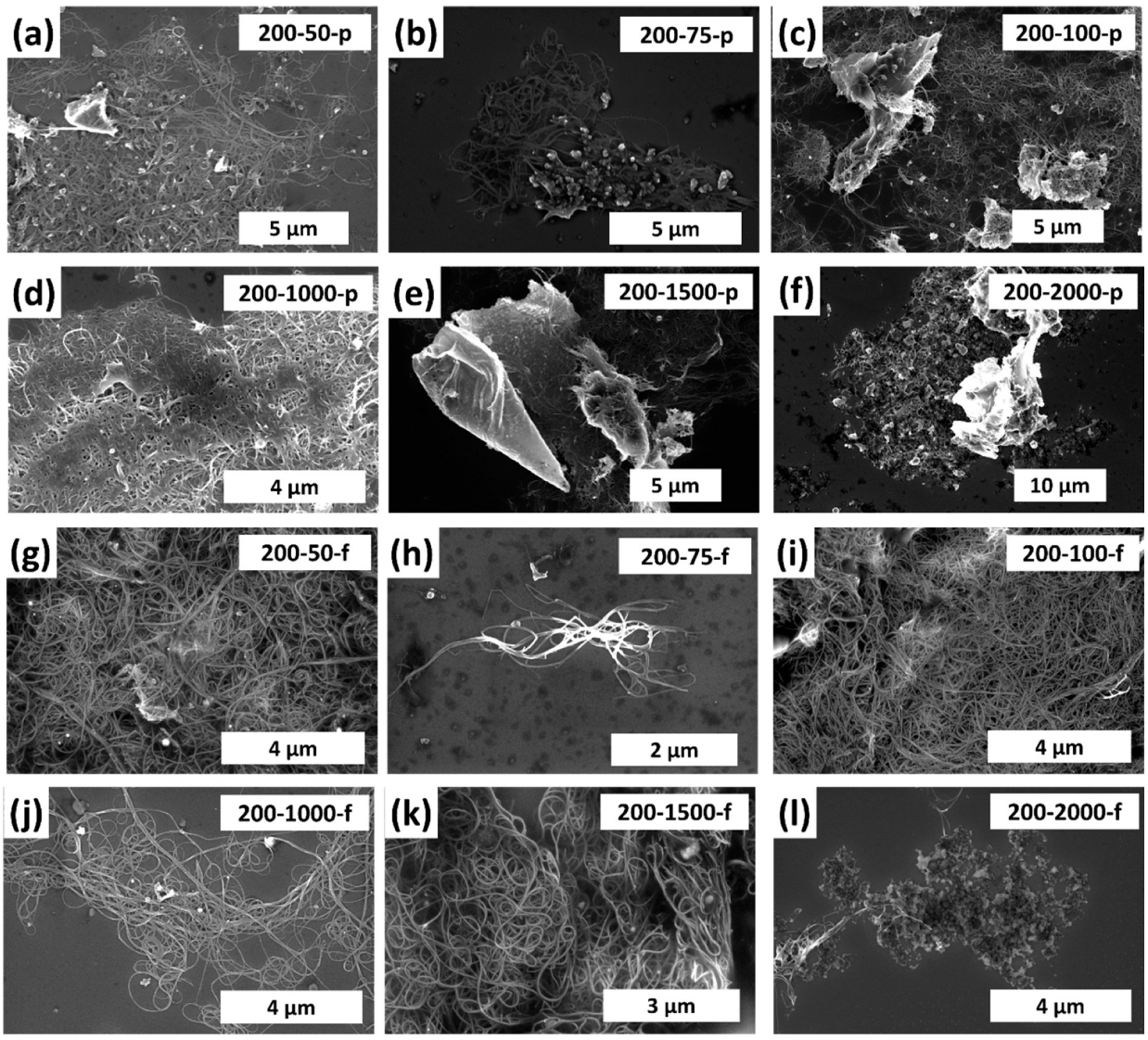

Figure 6. SEM images of powdery FJH Meijo SWCNT with pulse times of (a) 50, (b) 75, (c) 100, (d) 1000, (e) 1500, and (f) 2000 ms. SEM images of fibrous FJH Meijo SWCNT with pulse times of (g) 50, (h) 75, (i) 100, (j) 1000, (k) 1500, and (l) 2000 ms.

criteria: (1) a minimum I_{2D}/I_G ratio of 0.3, (2) a signal-to-noise ratio of >5 in the 2D band region, and (3) a 2D band with a fwhm of <100 cm^{-1}. Spectra were also analyzed using a custom-written MATLAB script to determine the relative proportions of pristine to nonpristine CNT. Spectra qualified as pristine CNT upon meeting two criteria: (1) a maximum I_D/I_G ratio of ≤0.05 and (2) a minimum I_{RBM}/I_G ratio of ≤0.04, where I_{RBM} is the greatest intensity value between 100 and 200 cm^{-1}. Spectra qualified as nonpristine CNT upon meeting two criteria: (1) a minimum I_D/I_G ratio of ≥0.05 and (2) a maximum I_{RBM}/I_G ratio of ≤0.1 to filter out noisy spectra.

Transmission Electron Microscopy (TEM). Dilute solutions with concentrations ∼1 mg mL^{-1} of each sample in ethanol were sonicated (Cole-Parmer 750-W ultrasonic processor with a cup horn) for 15 min before being drop cast onto a 200 mesh Cu grid with lacey carbon film. A JEOL 2100F field-emission gun TEM at 200 kV was then used to image the resulting sample. High-resolution TEM images were obtained using an FEI Titan base, 60−300 kV, equipped with a CEOS spherical aberration corrector for the objective lens, thereby assuring a spatial resolution of 1.2 Å at 80 kV. All experiments were performed at this voltage to minimize radiation damage.

Scanning Electron Microscopy (SEM). The same dilute solutions in ethanol were drop cast onto silicon wafers on a hot plate at ∼70 °C to remove the ethanol. The SEM images were then obtained with a FEI Helios NanoLab 660 DualBeam SEM system at 5.00 kV with a current of 0.1 nA.

Composite Preparation. DER 736 (3.0 g) was combined with 1,5-diamino-2-methylpentane (0.45 g) curing agent in a 20 mL scintillation vial, along with FJH SWCNT, SWCNT, or CG (at 30 mg, 15 mg, or 7.5 mg); the amount loaded depended on the desired wt % loading. The solution was then stirred at room temperature with a magnetic stir bar (30 min, 300 rpm). The solution was transferred to a cup−horn sonicator (Cole-Parmer 750-W ultrasonic processor with a cup horn) and sonicated (15 min at 50% amplitude) before being high shear mixed (15 min at ∼10 000 rpm) with a high shear mixer (Tissue Tearor 986370-07 Homogenizer; 120 VAC, 1.2 A). After it was degassed within a vacuum desiccator (1 h), the solution was cured, first, for 2 h at 70 °C and, then, at room temperature overnight. The scintillation vial with the cured composite was broken to release the material. The product was sanded using the face of an abrasive wheel and, then, 800, 1000, 1200, and 2500 grit sandpaper until it was the appropriate dimensions for microscale mechanical testing.

Triboindentation. Nanoindentation was carried out using a Hysitron TI 980 Triboindenter equipped with a Berkovich tip with a pyramidal geometry. To calculate the indentation modulus and hardness, at least 5 different indentations were performed for each sample with a maximum displacement of 500 nm and a displacement

https://doi.org/10.1021/acsnano.2c10125
ACS Nano 2023, 17, 2506−2516

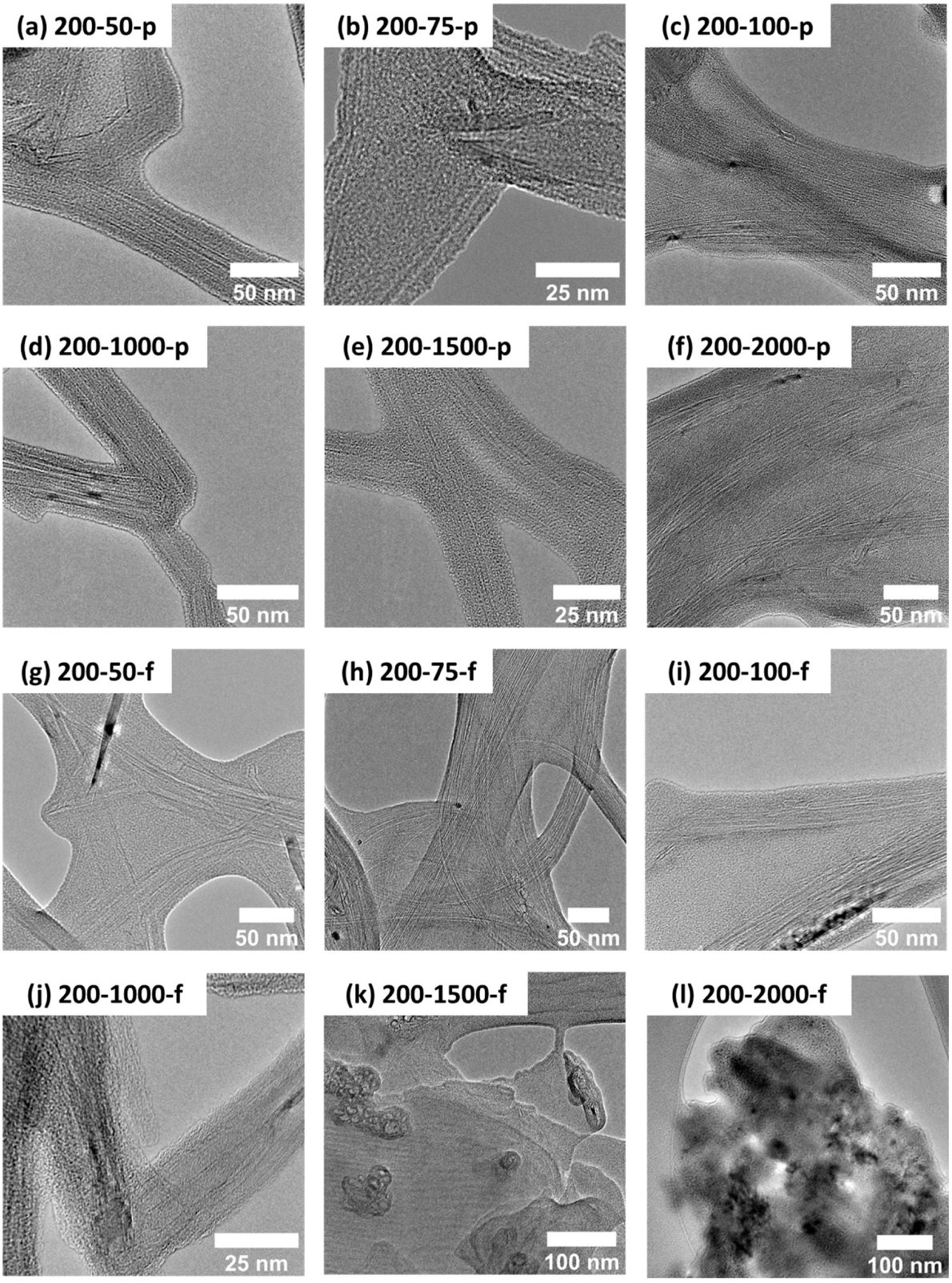

Figure 7. Representative TEM images of powdery FJH Meijo SWCNT with pulse times of (a) 50, (b) 75, (c) 100, (d) 1000, (e) 1500, and (f) 2000 ms. TEM images of fibrous FJH Meijo SWCNT with pulse times of (g) 50, (h) 75, (i) 100, (j) 1000, (k) 1500, and (l) 2000 ms.

rate of 10 nm s^{-1}. The elastic modulus and hardness were calculated using the Oliver−Pharr approach by employing eqs 1 −3.[32,33]

$$E_r = \frac{\sqrt{\pi}}{2}\frac{S}{\sqrt{A_p}} \quad (1)$$

$$\frac{1}{E_r} = \frac{1-\nu^2}{E} + \frac{1-\nu_i^2}{E_i} \quad (2)$$

$$H = \frac{P}{A_p} \quad (3)$$

https://doi.org/10.1021/acsnano.2c10125
ACS Nano 2023, 17, 2506−2516

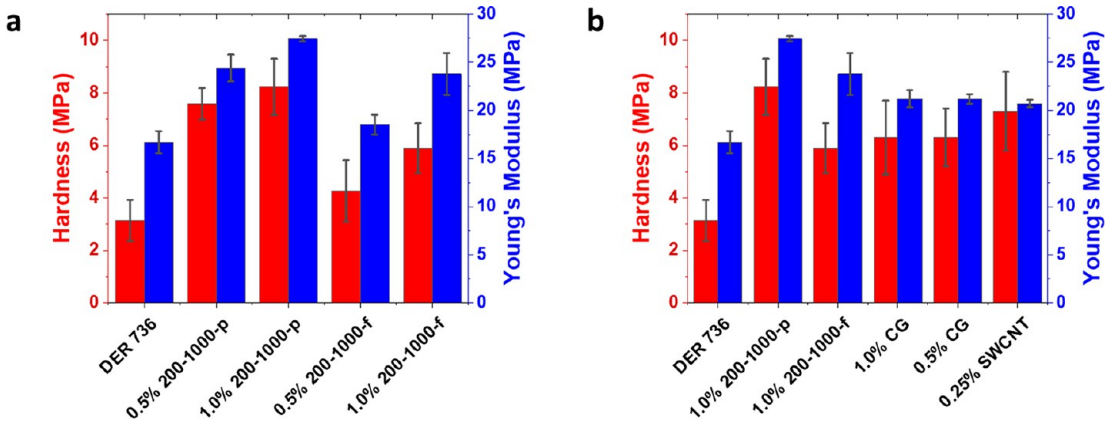

Figure 8. Characterization of microscale mechanical properties. Triboindentation results of epoxy composites with (a) 0.5% and 1% loading of FJH SWCNT (powdery and fibrous), as well as (b) 1% commercial graphene (CG), 0.5% CG, and 0.25% SWCNT.

where E_r is the reduced elastic modulus; S is the stiffness of the initial part of the unloading curve; A_P is the projected area of contact; E and ν are the elastic modulus and Poisson's ratio of the sample, respectively; E_i and ν_i are the elastic modulus and Poisson's ratio of the indenter, respectively; H is the hardness; and finally, P is the applied load.

Scanning Transmission Electron Microscopy (HAADF-STEM). The powdery and fibrous materials were treated with Cu etchant (Millipore-Sigma, Lot #: MKCP389) to remove excess Cu (from the FJH Cu electrodes) in the samples. Typically, Cu etchant solution (5 mL) was used to disperse 20 mg of each material. Each sample was sonicated for (30 min) to ensure dispersion and Cu etching. After the reaction, the sample was washed with deionized water to remove metal ions and neutralize the pH of the solution to near neutral. Aliquots of solution (20 μL) were then drop cast onto a 300 mesh Cu grid with lacey carbon film (Ted Pella, product number: 01883-F). The samples were then imaged under different magnifications with an aberration-corrected FEI Titan Themsis under a scanning transmission electron microscope (STEM) at 300 kV with a spot size of eight. A 25 mrad convergence angle was used with dwell times of 10 μs or higher.

UV−Vis Spectroscopy. A UV−vis spectrometer (Shimadzu UV-3600 Plus configured with a photomultiplier tube from 190 to 800 nm wavelength) was used to collect the spectra of the suspensions of reactant and FJH products. The SWCNT (2 to 10 mg mL^{-1}) were added to aqueous Pluronic F-127 (Lot #: BCCD0320, 1 wt % in deionized water). The mixture was bath-sonicated (Cole-Parmer 881) for 30 min to obtain a dispersion. The mixture was then allowed to settle for 1 week. The solution mixtures were not moved or shaken to avoid changes in concentration during this period. The supernatant was analyzed by UV−vis spectroscopy. The dispersions were diluted 100×, and the absorbance was recorded at 660 nm. An extinction coefficient of α_{660} = 6600 L g^{-1} m^{-1} was used to calculate the concentration of carbon materials in the aqueous solution.[31] The powdery product (2 to 6 mg mL^{-1}) and fibrous product (2 to 8 mg mL^{-1}) were analyzed using the same method above.

Electrical Measurement. Silver paste was coated on the top and bottom sides of the composites used for triboindentation as the electrodes for good electrical contact. The current was recorded with an Agilent B1500A semiconductor analyzer by scanning voltage from 0 to 0.1 V. The resistance was calculated accordingly. Resistivity of the sample was calculated on the basis of eq 4, where R is the resistance, ρ is the resistivity, L is the sample length, and S is the cross-sectional area.

$$R = \rho\frac{L}{S} \tag{4}$$

Temperature Measurement. The sample temperature during FJH was measured using the emitted blackbody spectrum. A Thorlabs Round-to-Linear optical fiber was mounted behind two Thorlabs air-spaced achromatic lenses to form a light-collecting assembly. This assembly was aligned and focused to the sample tube for optimal collection. The optical fiber was connected to a chamber with two plane mirrors and one thick diffracting mirror, such that the incoming light was diffracted onto a Hamamatsu S4111−16R silicon photodiode array. Each of the 16 channels on the array was connected to a custom printed circuit board in photovoltaic mode, and the voltage driven by the resulting photocurrent was amplified by operational amplifiers before being read by the analog channels of a National Instruments USB-6210 data acquisition device.

The wavelengths detected by the photodiode array were determined by aligning the spectral lines of a mercury UV lamp. The dark current and relative sensitivity of each photodiode channel were calibrated by aiming the collector at a 2900 K lamp, which was turned on and off. The dark current correction was simply the opposite of the voltage recorded with the lamp off, and the calibration coefficients were determined by fitting the shifted channel voltages to a 2900 K blackbody curve. Subsequent measurements were corrected using these two calibration parameters. Temperatures were calculated point-by-point by curve fitting each point's spectrum to a blackbody curve according to Planck's Law using the "curve_fit" function from the "scipy.optimize" Python package. This enabled measurement of temperatures in the range of approximately 1800−3500 K.

ASSOCIATED CONTENT

Supporting Information

The Supporting Information is available free of charge at https://pubs.acs.org/doi/10.1021/acsnano.2c10125.

Characterization of temperature during the FJH of SWCNT; Raman analyses; TEM images; SEM images; UV−vis characterization; and resistivity of composites made with additives (PDF)

AUTHOR INFORMATION

Corresponding Authors

Miguel Jose Yacaman − *Department of Applied Physics and Materials Science, Center for Materials Interfaces in Research and Applications, Northern Arizona University, Flagstaff, Arizona 86011, United States*; Email: miguel.yacaman@nau.edu

James M. Tour − *Department of Chemistry, Department of Materials Science and NanoEngineering, and Smalley-Curl Institute, NanoCarbon Center, and the Welch Institute for Advanced Materials, Rice University, Houston, Texas 77005, United States*; orcid.org/0000-0002-8479-9328; Email: tour@rice.edu

https://doi.org/10.1021/acsnano.2c10125
ACS Nano 2023, 17, 2506−2516

Authors

Paul A. Advincula − *Department of Chemistry, Rice University, Houston, Texas 77005, United States*

Jacob L. Beckham − *Department of Chemistry, Rice University, Houston, Texas 77005, United States*

Chi Hun Choi − *Department of Materials Science and NanoEngineering, Rice University, Houston, Texas 77005, United States*

Weiyin Chen − *Department of Chemistry, Rice University, Houston, Texas 77005, United States;* orcid.org/0000-0002-6427-4129

Yimo Han − *Department of Materials Science and NanoEngineering, Rice University, Houston, Texas 77005, United States;* orcid.org/0000-0003-0563-4611

Dmitry V. Kosynkin − *Department of Chemical and Biomolecular Engineering, Rice University, Houston, Texas 77005, United States*

Alexander Lathem − *Department of Chemistry and Smalley-Curl Institute, NanoCarbon Center, and the Welch Institute for Advanced Materials, Rice University, Houston, Texas 77005, United States*

Alvaro Mayoral − *Instituto de Nanociencia y Materiales de Aragon (INMA), Spanish National Research Council (CSIC), University of Zaragoza, 50009 Zaragoza, Spain; Laboratorio de Microscopias Avanzadas (LMA), Universidad de Zaragoza, 50018 Zaragoza, Spain; Center for High-Resolution Electron Microscopy (ChEM), School of Physical Science and Technology, ShangaiTech University, Shangai 201210, China;* orcid.org/0000-0002-5229-2717

Complete contact information is available at: https://pubs.acs.org/10.1021/acsnano.2c10125

Notes

The authors declare the following competing financial interest(s): Rice University owns intellectual property on the synthesis and use of FG. That intellectual property has been licensed to a company in which JMT is a stockholder, but not an officer, director, or employee. Conflicts of interest are mitigated through regular disclosure to and compliance with the Rice University Office of Sponsored Programs and Research Compliance. The other authors declare no other conflicts.

ACKNOWLEDGMENTS

The Air Force Office of Scientific Research (FA9550-22-1-0526) and the U.S. Army Corps of Engineers, ERDC (W912HZ-21-2-0050), funded this work. J.L.B. acknowledges support from the NSF Graduate Research Fellowship Program. A.M. acknowledges the Spanish Ministry of Science through the Ramón y Cajal program (RYC2018-024561-I), the regional government of Aragon (DGA E13-20R), and also acknowledges the National Natural Science Foundation of China (NSFC-21835002). Y.H. and C.-H.C. acknowledge support from the Welch Foundation (C-2065-20210327). This work utilized the instruments in the Electron Microscopy Center at Rice University.

REFERENCES

(1) Nadiv, R.; Shtein, M.; Buzaglo, M.; Peretz-Damari, S.; Kovalchuk, A.; Wang, T.; Tour, J. M.; Regev, O. Graphene Nanoribbon-Polymer Composites: The Critical Role of Edge Functionalization. *Carbon* **2016**, *99*, 444−450.

(2) Rafiee, M. A.; Lu, W.; Thomas, A. V.; Zandiatashbar, A.; Rafiee, J.; Tour, J. M.; Koratkar, N. A. Graphene Nanoribbon Composites. *ACS Nano* **2010**, *4*, 7415−7420.

(3) Raji, A. R. O.; Varadhachary, T.; Nan, K.; Wang, T.; Lin, J.; Ji, Y.; Genorio, B.; Zhu, Y.; Kittrell, C.; Tour, J. M. Composites of Graphene Nanoribbon Stacks and Epoxy for Joule Heating and Deicing of Surfaces. *ACS Appl. Mater. Interfaces* **2016**, *8*, 3551−3556.

(4) Joshi, A.; Bajaj, A.; Singh, R.; Anand, A.; Alegaonkar, P. S.; Datar, S. Processing of Graphene Nanoribbon Based Hybrid Composite for Electromagnetic Shielding. *Compos. Part B Eng.* **2015**, *69*, 472−477.

(5) Mondal, S.; Ghosh, S.; Raj, C. R. Unzipping of Single-Walled Carbon Nanotube for the Development of Electrocatalytically Active Hybrid Catalyst of Graphitic Carbon and Pd Nanoparticles. *ACS Omega* **2018**, *3*, 622−630.

(6) Jeong, Y. C.; Lee, K.; Kim, T.; Kim, J. H.; Park, J.; Cho, Y. S.; Yang, S. J.; Park, C. R. Partially Unzipped Carbon Nanotubes for High-Rate and Stable Lithium-Sulfur Batteries. *J. Mater. Chem. A* **2016**, *4*, 819−826.

(7) Zhang, E.; Wang, J.; Wang, B.; Yu, X.; Yang, H.; Lu, B. Unzipped Carbon Nanotubes for Aluminum Battery. *Energy Storage Mater.* **2019**, *23*, 72−78.

(8) Geim, A. K.; Novoselov, K. S. The Rise of Graphene. *Nat. Mater.* **2007**, *6*, 183−191.

(9) Wang, T.; Wang, Z.; Salvatierra, R. V.; McHugh, E.; Tour, J. M. Top-down Synthesis of Graphene Nanoribbons Using Different Sources of Carbon Nanotubes. *Carbon* **2020**, *158*, 615−623.

(10) Kosynkin, D. V.; Higginbotham, A. L.; Sinitskii, A.; Lomeda, J. R.; Dimiev, A.; Price, B. K.; Tour, J. M. Longitudinal Unzipping of Carbon Nanotubes to Form Graphene Nanoribbons. *Nature* **2009**, *458*, 872−876.

(11) Kosynkin, D. V.; Lu, W.; Sinitskii, A.; Pera, G.; Sun, Z.; Tour, J. M. Highly Conductive Graphene Nanoribbons by Longitudinal Splitting of Carbon Nanotubes Using Potassium Vapor. *ACS Nano* **2011**, *5*, 968−974.

(12) Yu, D.; Dai, L. Self-Assembled Graphene/Carbon Nanotube Hybrid Films for Supercapacitors. *J. Phys. Chem. Lett.* **2010**, *1*, 467−470.

(13) Dong, X.; Li, B.; Wei, A.; Cao, X.; Chan-Park, M. B.; Zhang, H.; Li, L. J.; Huang, W.; Chen, P. One-Step Growth of Graphene-Carbon Nanotube Hybrid Materials by Chemical Vapor Deposition. *Carbon* **2011**, *49*, 2944−2949.

(14) Ozden, S.; Autreto, P. A. S.; Tiwary, C. S.; Khatiwada, S.; Machado, L.; Galvao, D. S.; Vajtai, R.; Barrera, E. V.; M. Ajayan, P. Unzipping Carbon Nanotubes at High Impact. *Nano Lett.* **2014**, *14*, 4131−4137.

(15) Wang, C.; Zhao, Y.; Zhang, Y.; Miao, L.; Wu, J.; Yang, Y.; Xu, Z.; Peng, Q.; He, X.; Sui, C. Partially Unzipping Carbon Nanotubes: A Route to Synchronously Improve Fracture Strength and Toughness of Nanocomposites Inspired by Pinning Effect of Screw. *Mater. Today Commun.* **2020**, *25*, 101355.

(16) Hacopian, E. F.; Yang, Y.; Ni, B.; Li, Y.; Li, X.; Chen, Q.; Guo, H.; Tour, J. M.; Gao, H.; Lou, J. Toughening Graphene by Integrating Carbon Nanotubes. *ACS Nano* **2018**, *12*, 7901−7910.

(17) Lee, J. H.; Rhee, K. Y.; Park, S. J. Silane Modification of Carbon Nanotubes and Its Effects on the Material Properties of Carbon/CNT/Epoxy Three-Phase Composites. *Compos. Part A Appl. Sci. Manuf.* **2011**, *42*, 478−483.

(18) Salvatierra, R. V.; Zakhidov, D.; Sha, J.; Kim, N. D.; Lee, S. K.; Raji, A. R. O.; Zhao, N.; Tour, J. M. Graphene Carbon Nanotube Carpets Grown Using Binary Catalysts for High-Performance Lithium-Ion Capacitors. *ACS Nano* **2017**, *11*, 2724−2733.

(19) Yan, Z.; Peng, Z.; Casillas, G.; Lin, J.; Xiang, C.; Zhou, H.; Yang, Y.; Ruan, G.; Raji, A. R. O.; Samuel, E. L. G.; Hauge, R. H.; Yacaman, M. J.; Tour, J. M. Rebar Graphene. *ACS Nano* **2014**, *8*, 5061−5068.

(20) Zhu, Y.; Li, L.; Zhang, C.; Casillas, G.; Sun, Z.; Yan, Z.; Ruan, G.; Peng, Z.; Raji, A. R. O.; Kittrell, C.; Hauge, R. H.; Tour, J. M. A Seamless Three-Dimensional Carbon Nanotube Graphene Hybrid Material. *Nat. Commun.* **2012**, *3*, 1225.

(21) Yan, Z.; Ma, L.; Zhu, Y.; Lahiri, I.; Hahm, M. G.; Liu, Z.; Yang, S.; Xiang, C.; Lu, W.; Peng, Z.; Sun, Z.; Kittrell, C.; Lou, J.; Choi, W.; Ajayan, P. M.; Tour, J. M. Three-Dimensional Metal- Graphene-Nanotube Multifunctional Hybrid Materials. *ACS Nano* **2013**, *7*, 58−64.
(22) Chen, W.; Li, J. T.; Wang, Z.; Algozeeb, W. A.; Luong, D. X.; Kittrell, C.; McHugh, E. A.; Advincula, P. A.; Wyss, K. M.; Beckham, J. L.; Stanford, M. G.; Jiang, B.; Tour, J. M. Ultrafast and Controllable Phase Evolution by Flash Joule Heating. *ACS Nano* **2021**, *15*, 11158−11167.
(23) Chen, W.; Li, J. T.; Ge, C.; Yuan, Z.; Algozeeb, W. A.; Advincula, P. A.; Gao, G.; Chen, J.; Ling, K.; Choi, C. H.; McHugh, E. A.; Wyss, K. M.; Luong, D. X.; Wang, Z.; Han, Y.; Tour, J. M. Turbostratic Boron-Carbon-Nitrogen and Boron-Nitride by Flash Joule Heating. *Adv. Mater.* **2022**, *34*, 2202666.
(24) Advincula, P. A.; Luong, D. X.; Chen, W.; Raghuraman, S.; Shahsavari, R.; Tour, J. M. Flash Graphene from Rubber Waste. *Carbon* **2021**, *178*, 649−656.
(25) Wyss, K. M.; Beckham, J. L.; Chen, W.; Luong, D. X.; Hundi, P.; Raghuraman, S.; Shahsavari, R.; Tour, J. M. Converting Plastic Waste Pyrolysis Ash into Flash Graphene. *Carbon* **2021**, *174*, 430−438.
(26) Algozeeb, W. A.; Savas, P. E.; Luong, D. X.; Chen, W.; Kittrell, C.; Bhat, M.; Shahsavari, R.; Tour, J. M. Flash Graphene from Plastic Waste. *ACS Nano* **2020**, *14*, 15595−15604.
(27) Beckham, J. L.; Wyss, K. M.; Xie, Y.; McHugh, E. A.; Li, J. T.; Advincula, P. A.; Chen, W.; Lin, J.; Tour, J. M. Machine Learning Guided Synthesis of Flash Graphene. *Adv. Mater.* **2022**, *34*, 2106506.
(28) Yao, Y.; Fu, K. K.; Zhu, S.; Dai, J.; Wang, Y.; Pastel, G.; Chen, Y.; Li, T.; Wang, C.; Li, T.; Hu, L. Carbon Welding by Ultrafast Joule Heating. *Nano Lett.* **2016**, *16*, 7282−7289.
(29) Terrones, M.; Terrones, H.; Banhart, F.; Charlier, J.-C.; Ajayan, P. M. Coalescence of Single-Walled Carbon Nanotubes. *Science* **2000**, *288*, 1226−1229.
(30) Stanford, M. G.; Bets, K. V.; Luong, D. X.; Advincula, P. A.; Chen, W.; Li, J. T.; Wang, Z.; McHugh, E. A.; Algozeeb, W. A.; Yakobson, B. I.; Tour, J. M. Flash Graphene Morphologies. *ACS Nano* **2020**, *14*, 13691−13699.
(31) Luong, D. X.; Bets, K. V.; Algozeeb, W. A.; Stanford, M. G.; Kittrell, C.; Chen, W.; Salvatierra, R. V.; Ren, M.; McHugh, E. A.; Advincula, P. A.; Wang, Z.; Bhatt, M.; Guo, H.; Mancevski, V.; Shahsavari, R.; Yakobson, B. I.; Tour, J. M. Gram-Scale Bottom-up Flash Graphene Synthesis. *Nature* **2020**, *577*, 647−651.
(32) Han, X.; Wang, T.; Owuor, P. S.; Hwang, S. H.; Wang, C.; Sha, J.; Shen, L.; Yoon, J.; Wang, W.; Salvatierra, R. V.; Ajayan, P. M.; Shahsavari, R.; Lou, J.; Zhao, Y.; Tour, J. M. Ultra-Stiff Graphene Foams as Three-Dimensional Conductive Fillers for Epoxy Resin. *ACS Nano* **2018**, *12*, 11219−11228.
(33) Oliver, W. C.; Pharr, G. M. An Improved Technique for Determining Hardness and Elastic Modulus Using Load and Displacement Sensing Indentation Experiments. *J. Mater. Res.* **1992**, *7*, 1564−1583.

https://doi.org/10.1021/acsnano.2c10125
ACS Nano 2023, 17, 2506−2516